Two-dimensional self-consistent radiation transport model for plasma display panels

Hae June Lee,[a] Hyun Chul Kim, Sung Soo Yang, and Jae Koo Lee
Department of Electronic and Electrical Engineering, Pohang University of Science and Technology, Pohang 790-784, South Korea

(Received 23 October 2001; accepted 26 February 2002)

A two-dimensional radiation transport model is coupled with a fluid simulation to incorporate the resonance radiation trapping effect in a plasma display panel cell. Compared with the conventional trapping factor approach, this model has an advantage in describing the spatial evolution of the radiative excited-state density. Compared with a Monte Carlo model, it also takes advantage of its fast computation to couple the radiation transport self-consistently with the time-dependent fluid model. The effect of the spatial evolution of the resonant excited state on the light emission is investigated for the variations of system sizes and the gas mixture ratio, and the results are compared with those of the conventional trapping factor approach. The discrepancy between the two methods increases as the gap size between the dielectrics increases, but does not change significantly for the variation of the gas mixture ratio. © *2002 American Institute of Physics.*
[DOI: 10.1063/1.1470498]

I. INTRODUCTION

Plasma discharges have many applications as light sources with ultraviolet (UV) emissions from excited states. Fluorescent lamps, dielectric barrier discharges, and excimer lasers are the most common examples. Recently, plasmas have also been applied as a promising candidate for a large area flat display device, the plasma display panel (PDP).[1–4] It is one of the leading candidates for large screen (more than 40 inches) high definition television display. However, the luminous efficiency of the PDP is still very low with current technology, less than 3 lm/W.

In these systems, the photons emitted from resonant excited states are absorbed by ground-state atoms, and these emission and absorption processes may be repeated many times until the photon finally escapes the system. This phenomenon is called *resonance radiation trapping*. By this process, the apparent radiative decay time becomes much longer than the vacuum radiative decay time and the emission spectra change significantly. Therefore, the radiation trapping effect plays an important role in light source devices using resonance radiation, and is critical for the calculation of radiation efficiency.

One of the most dominant lines in a PDP cell is the 147 nm UV light from the Xe $6s\ ^3P_1$ resonant excited state, which is optically thick. Therefore, a proper simulation model for the resonance radiation trapping is necessary in order to describe the resonant state accurately. The simplest method is to use the effective decay rate with the trapping factor of the lowest eigenmode solution of Holstein's equation.[5] This method is adequate if the spatial distribution of the radiative excited-state density is close to the lowest eigenmode solution, but cannot represent the redistribution of the excited-state density by the radiation trapping effect.

Another method is to treat the problem with the Monte Carlo (MC) photon simulation,[6–8] which is useful for arbitrary line shapes and any complex geometry. The MC method, however, is not self-consistently coupled with plasma motions because of its expensive computation cost. To overcome this difficulty, Lawler *et al.* developed a numerical method called the propagator function method (PFM),[9] which solves Holstein's equation in a way similar to fluid models by adding the radiation transport (RT) with a kernel function. This method is faster than the MC method and capable of calculating the time-dependent evolution of the radiative state self-consistently.

Sahni *et al.*[10] reported a one-dimensional planar model similar to the PFM for the RT in a PDP-like discharge between two insulated metal electrodes with a Ne–Ar gas mixture. They used an asymptotic expression for Holstein's equation with high opacity assumption for pressure broadening and assumed uniform background gas density.

Recently, Lee and Verboncoeur reported a RT model using the PFM coupled with a particle-in-cell model (RT-PIC)[11] for the application to the simulation of one-dimensional planar[12] and cylindrical positive column[13] glow discharges. Here, electrons and ions are treated with the conventional particle-in-cell method,[14] and neutral atoms are simulated with a fluid model including time-dependent RT with Holstein's equation for the resonant state. The model treated both Doppler and pressure broadenings and the effect of nonuniform ground state density. It was found that the trapping factor approach (TFA) is not valid when the lowest eigenmode of Holstein's solution cannot represent the exact excited-state density profile.

In this study, we introduce a two-dimensional RT model coupled with a fluid simulation using the PFM to describe

[a]Present address: Korea Electrotechnology Research Institute, Changwon 641-120, South Korea; electronic mail: leehj@keri.re.kr

 © 2002 American Institute of Physics

Downloaded 12 Jun 2002 to 141.223.180.14. Redistribution subject to AIP license or copyright, see http://ojps.aip.org/pop/popcr.jsp

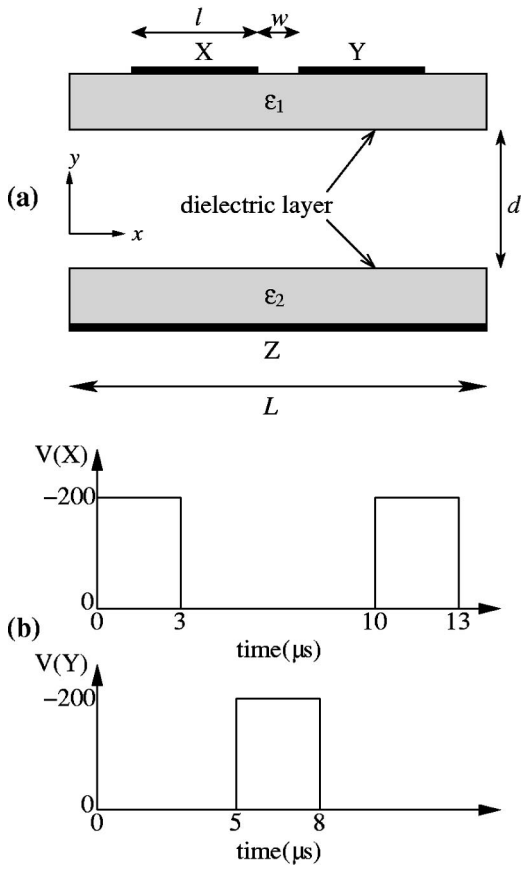

FIG. 1. (a) A PDP cell diagram for the two-dimensional model considered in the calculations. The dielectric on the top with sustain electrodes corresponds to the front plate of the display panel, and the phosphors are deposited on the surface of the bottom dielectric. (b) Pulse shapes of the applied voltages biased at the sustain electrodes (X and Y). The potential of the address electrode (Z) is set to zero after the matrix discharge during the first 3 μs.

the production of UV radiation in PDP discharges properly. We describe the two-dimensional Cartesian RT model in Sec. II, followed by simulation results for the variations of system size and gas mixture in Sec. III. The results are also compared with those with the TFA in Sec. III. Finally, summary and discussions are presented in Sec. IV.

II. DESCRIPTION OF THE MODEL

The basis of this study is a two-dimensional fluid code for a PDP cell, FL2P.[15] A cell geometry and applied pulse shapes are shown in Fig. 1. The governing equations are the continuity equation, the momentum equation with drift-diffusion approximation, and Poisson's equation as conventional methods.[16,17] The model treats mixtures of three gas species, Xe, Ne, and He. It includes six excited states of Xe [i.e., $Xe^*(^3P_2)$, $Xe^*(^3P_1)$, $Xe_2^*(O_u^+)$, $Xe_2^*(^3\Sigma_u^+)$, $Xe_2^*(^1\Sigma_u^+)$, and Xe**], and emission spectra from the radiative excited states (i.e., 147, 150, 173, and 828 nm). Collisions between neutral species and Penning ionization are included, as well as the electron impact ionizations and excitations. The code also has been extended to a three-dimensional model[18] to investigate the effects of electrode structures and barrier ribs.

In this study, we consider the radiation trapping of the photons emitted from the $Xe^*(^3P_1)$ resonant state with a wavelength of 147 nm. The RT equation is included with the PFM.[9] The neutral gas density profile is assumed to be uniform, which is valid for the pressure regime concerned. Because the cell is operated at high pressure ($\sim$500 Torr), pressure broadening with a Lorentz line shape is dominant. Moreover, we assume that the frequency of a re-emitted photon is completely independent of that of the absorbed photon. The details of the RT model can be obtained in the previous works.[11–13]

The governing equation of the resonant state density is the modified Holstein equation

$$\frac{\partial n^*(\mathbf{r},t)}{\partial t}+\nabla\cdot\mathbf{\Gamma}(\mathbf{r},t)=P(\mathbf{r},t)-\frac{1}{\tau_v}n^*(\mathbf{r},t)+\frac{1}{\tau_v}\int n^*(\mathbf{r}',t)G(\mathbf{r},\mathbf{r}')d\mathbf{r}', \quad (1)$$

where $n^*(\mathbf{r},t)$, $\mathbf{\Gamma}(\mathbf{r},t)$, and $P(\mathbf{r},t)$ are the resonant state density, particle flux, and the production rate, respectively. τ_v is the vacuum radiative decay time, which is 3.56 ns for the $Xe^*(^3P_1)$ state. $G(\mathbf{r},\mathbf{r}')$ is the kernel function, which is the probability for a resonance photon emitted at the position $\mathbf{r}'$ to be absorbed at the position $\mathbf{r}$.

The kernel function is calculated from the transmission factor $T(\mathbf{r},\mathbf{r}')$ as

$$G(\mathbf{r},\mathbf{r}')=-\frac{\mathbf{R}}{4\pi R^3}\cdot\nabla_{\mathbf{r}}T(\mathbf{r},\mathbf{r}'), \quad (2)$$

where $\mathbf{R}=\mathbf{r}-\mathbf{r}'$ and $R=|\mathbf{R}|$. For uniform ground-state density, the transmission factor depends only on the distance between two positions $\mathbf{r}$ and $\mathbf{r}'$, and therefore, it is shift invariant and isotropic in Cartesian coordinate. Therefore,

$$T(\mathbf{r},\mathbf{r}')=T(R)=\int_0^\infty g(\nu)\exp[-k(\nu)R]d\nu. \quad (3)$$

Here, $g(\nu)$ and $k(\nu)$ are the line shape and the absorption coefficient, respectively,

$$k(\nu)=\frac{\lambda_0^2}{8\pi\tau_v}\frac{g_2}{g_1}n_{\mathrm{Xe}}g(\nu) \quad (4)$$

and

$$g(\nu)=\frac{\Delta\nu^L/2\pi}{(\nu-\nu_0)^2+(\Delta\nu^L/2)^2}, \quad (5)$$

for the Lorentz line shape by pressure broadening. Here, λ_0 is the wavelength at the line center, g_1 and g_2 are the degeneracies of lower and upper states, respectively, ν_0 is the frequency at the line center, and $\Delta\nu^L$ is the linewidth defined as the FWHM (full width at half maximum) of the line shape. We define the peak absorption coefficient k_0 at the line center as

$$k_0=\frac{\lambda_0^2}{8\pi\tau_v}\frac{g_2}{g_1}\frac{2}{\pi\Delta\nu^L}n_{\mathrm{Xe}}. \quad (6)$$

Downloaded 12 Jun 2002 to 141.223.180.14. Redistribution subject to AIP license or copyright, see http://ojps.aip.org/pop/popcr.jsp

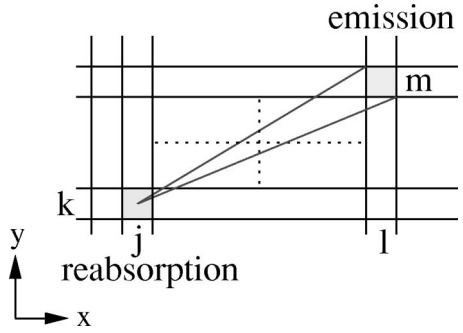

FIG. 2. Simulation mesh diagram of radiation transport for a photon emitted at (l,m)th cell to be reabsorbed at the (j,k)th cell. With the piecewise-constant approximation, the density at each cell is assumed to be constant.

From experimental data for Xe–Ne gas mixture,[19] the linewidth is

$$\Delta\nu^L = 4.06\times 10^{-15} n_{\mathrm{Xe}} + 1.6\times 10^{-16} n_{\mathrm{Ne}}, \tag{7}$$

where n_{Xe} and n_{Ne} are the densities of Xe and Ne gases, respectively. In this study, we consider only Ne–Xe mixture without He species.

With a piecewise constant approximation (PCA), the last term in Eq. (1) becomes

$$\int n^*(\mathbf{r}',t)G(\mathbf{r}_{jk},\mathbf{r}')d\mathbf{r}' = \sum_{l=1}^{N_x}\sum_{m=1}^{N_y} n^*_{lm}(t)\int_{lm} G(\mathbf{r}_{jk},\mathbf{r}')d\mathbf{r}', \tag{8}$$

where $\mathbf{r}_{jk}$ is the center position of the (j,k)th cell N_x and N_y are the numbers of cells in x and y directions, and n^*_{lm} is the constant density at the (l,m)th cell shown in Fig. 2.

We define the radiation transport matrix $A_{jk;lm}$ as the spatial integral of the kernel function over the volume of the (l,m)th cell

$$A_{jk;lm} \equiv \int_{lm} G(\mathbf{r}_{jk},\mathbf{r}')d\mathbf{r}', \tag{9}$$

which is the probability for a photon emitted within the (l,m)th cell to be reabsorbed at the center of the (j,k)th cell. For resonance collision broadening with a high opacity, $k_0R>100$, the equation is simplified by analytic calculations

$$A_{jk;lm} = \delta_{jl}\delta_{km} + A^{(a)}_{|j-l|,|k-m|} + A^{(b)}_{|j-l|,|k-m|} + A^{(c)}_{|j-l|,|k-m|} + A^{(d)}_{|j-l|,|k-m|}, \tag{10}$$

where $A^{(a)}_{|j-l|,|k-m|}$, $A^{(a)}_{|j-l|,|k-m|}$, $A^{(a)}_{|j-l|,|k-m|}$, and $A^{(a)}_{|j-l|,|k-m|}$ are surface integral segments at the top, the right-hand side, the left-hand side, and the bottom surfaces of the (l,m)th cell, respectively,

$$A^{(a)}_{|j-l|,|k-m|} = -\frac{\Delta y(|k-m|+1/2)}{12\pi^2\sqrt{2k_0}}\Gamma^2\left(\frac{1}{4}\right) \times \int_{(|j-l|-1/2)\Delta x}^{(|j-l|+1/2)\Delta x}\left[x^2+\Delta y^2\left(|k-m|+\frac{1}{2}\right)^2\right]^{-5/4} dx, \tag{11}$$

$$A^{(b)}_{|j-l|,|k-m|} = -\frac{\Delta x(|j-l|+1/2)}{12\pi^2\sqrt{2k_0}}\Gamma^2\left(\frac{1}{4}\right) \times \int_{(|k-m|-1/2)\Delta y}^{(|k-m|+1/2)\Delta y}\left[y^2+\Delta x^2\left(|j-l|+\frac{1}{2}\right)^2\right]^{-5/4} dy, \tag{12}$$

$$A^{(c)}_{|j-l|,|k-m|} = \frac{\Delta y(|k-m|-1/2)}{12\pi^2\sqrt{2k_0}}\Gamma^2\left(\frac{1}{4}\right) \times \int_{(|j-l|-1/2)\Delta x}^{(|j-l|+1/2)\Delta x}\left[x^2+\Delta y^2\left(|k-m|-\frac{1}{2}\right)^2\right]^{-5/4} dx, \tag{13}$$

and

$$A^{(d)}_{|j-l|,|k-m|} = \frac{\Delta x(|j-l|-1/2)}{12\pi^2\sqrt{2k_0}}\Gamma^2\left(\frac{1}{4}\right) \times \int_{(|k-m|-1/2)\Delta y}^{(|k-m|+1/2)\Delta y}\left[y^2+\Delta x^2\left(|j-l|+\frac{1}{2}\right)^2\right]^{-5/4} dy. \tag{14}$$

The derivation is described in Appendix A.

From the self-consistent evolution of radiative state density profile, the spectral radiation flux $F(\mathbf{r},\nu)$ and total radiation flux $F(\mathbf{r})$ can be calculated with the PCA. At the phosphor surface (x_i,y_0)

$$F(x_i,\nu) = \sum_{j=1}^{N_x}\sum_{k=1}^{N_y} n^*_{jk}\tilde{F}^{\nu}_{|i-j|,k}, \tag{15}$$

where

$$\tilde{F}^{\nu}_{|i-j|,k} = \frac{g(\nu)}{4\pi\tau_v}\int_{x_j-\Delta x/2}^{x_j+\Delta x/2}\int_{y_k-\Delta y/2-y_0}^{y_k+\Delta y/2-y_0} y' \times \frac{Ki_2[k(\nu)\sqrt{(x_i-x')^2+y'^2}]}{(x_i-x')^2+y'^2}dy'dx', \tag{16}$$

if $y_k-y_0 \leqslant \Delta y$ or $|i-j|\leqslant 1$, and

$$\tilde{F}^{\nu}_{|i-j|,k} = \frac{g(\nu)}{4\pi\tau_v}\Delta x\Delta y(y_k-y_0) \times \frac{Ki_2[k(\nu)\sqrt{(x_j-x_i)^2+(y_k-y_0)^2}]}{(x_j-x_i)^2+(y_k-y_0)^2}, \tag{17}$$

otherwise. Here, $Ki_2(u)$ is the second repeated integral of the zeroth-order modified Bessel function, $K_0(u)$.[20]

In a similar way, the total radiation flux at the phosphor surface is

$$F(x_i) = \sum_{j=1}^{N_x}\sum_{k=1}^{N_y} n^*_{jk}F_{|i-j|,k}, \tag{18}$$

where

Downloaded 12 Jun 2002 to 141.223.180.14. Redistribution subject to AIP license or copyright, see http://ojps.aip.org/pop/popcr.jsp

TABLE I. Simulation parameters.

Gap distance (d)	125–250 μm
Cell length (L)	1260 μm
Electrode length (l)	380 μm
Electrode gap width (w)	60 μm
Gas pressure	500 Torr
Xe mole fraction	1%–10%
Applied pulse period	5 μs
Applied pulse duration	3 μs
Applied pulse voltage	200 V
Vacuum radiative decay time (τ_v)	3.56 ns
Linewidth ($\Delta\nu^L$)	2.7–7.6 GHz
Absorption coefficient (k_0)	2.3–8.4$\times 10^5$ cm^{-1}

$$F_{|i-j|,k}=\frac{\Gamma^2(1/4)}{6\pi^2\tau_v\sqrt{2k_0}} \times\int_0^{\Delta x/2}\{[(|x_i-x_j|+x')^2+(y_k-y_0)^2]^{-1/4} +[(|x_i-x_j|-x')^2+(y_k-y_0)^2]^{-1/4} -[(|x_i-x_j|+x')^2+(y_k-y_0+\Delta y)^2]^{-1/4} -[(|x_i-x_j|-x')^2+(y_k-y_0+\Delta y)^2]^{-1/4}\}dx'. \quad (19)$$

The derivations of Eqs. (15)–(19) are described in Appendices B and C.

III. SIMULATION RESULTS

We simulated a PDP cell with the variations of the system size and the mole fraction of Ne–Xe mixture. The structure of the cell and the pulse shapes are shown in Fig. 1 and the simulation parameters are listed in Table I. The address electrode (Z) shown in Fig. 1(a) is biased to have 108 V only for the first 3 μs to trigger matrix discharge between upper and lower plates, and set to zero after then. The sustain electrodes (X) and (Y) have repeated pulses with period of 10 μs and duration of 3 μs alternately, as shown in Fig. 1(b). Therefore, from the second discharge after 5 μs, coplanar discharge is generated and the discharge has a density peak near the center of the front plate.

The time evolutions of the densities of electrons, Ne^+ and Xe^+ ions, and the Xe*($^3P_1$) excited state are shown in Fig. 3. The first discharge is triggered between the (X) and (Z) electrodes (called matrix discharge) and extinguished within a few microseconds because of the accumulated wall charge on the dielectrics. The second discharge is triggered between the (X) and (Y) electrodes (called coplanar discharge) and needs less voltage difference between two electrodes compared with the previous one because of the preaccumulated wall charge on the (X) electrode.

The Xe^+ density is much higher than that of Ne^+ even though the mole fraction of Xe gas (4%) is much lower than that of Ne (96%). This is due to the lower ionization cross-section of Ne gas. Moreover, it is noticeable that the decay time of the Xe*($^3P_1$) state shown in Fig. 3 is much slower than the vacuum radiative decay time, $\tau_v=3.56$ ns, which is

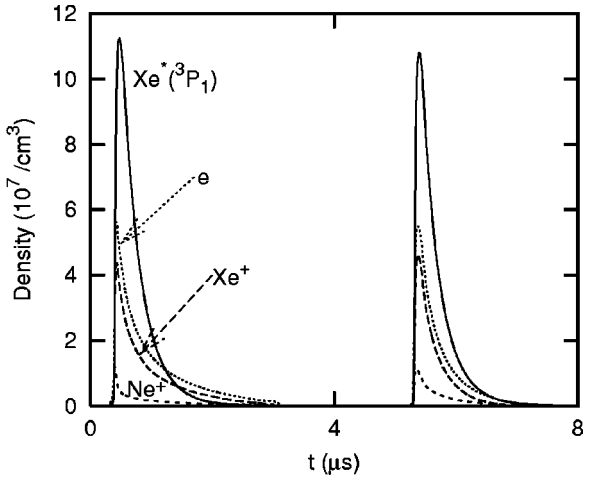

FIG. 3. Time evolutions of the spatially averaged densities of Xe*($^3P_1$), Ne^+, Xe^+, and electrons. The first discharge is triggered by the potential difference between (X) and (Z) electrodes shown in Fig. 1(a) and the second one is sustained by the potential difference between (X) and (Y) electrodes. $d=125$ μm and 4% of Xe mole fraction are used.

caused by the radiation trapping effect. The trapping factor is defined as the average number of absorption-reemission events of a photon emitted at a certain position before it reaches system boundary.

Figure 4 shows the trapping factor profile and its time evolution averaged over the system volume for the case with 4% of Xe mole fraction and $d=125$ μs. From the kernel function calculation, Eq. (A6), we can derive the equation for the trapping factor calculated in this model as

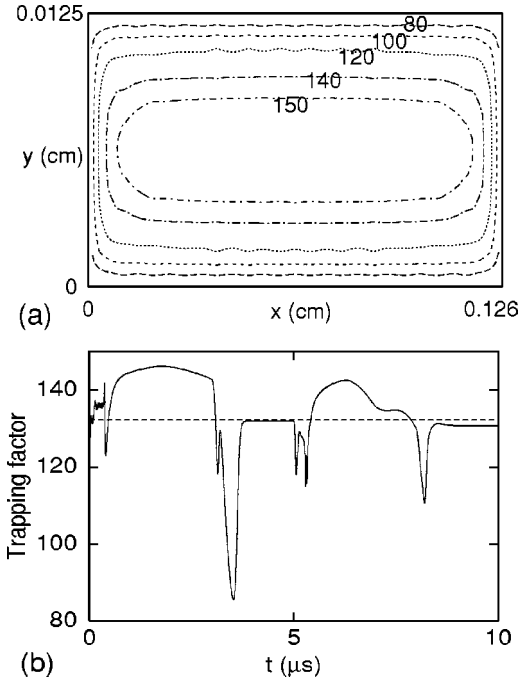

FIG. 4. (a) A trapping factor profile calculated by Eq. (20) in discharge space and (b) spatially averaged trapping factor calculated from Eq. (22) (solid) and the constant trapping factor calculated from Eq. (21), $g_0=132$ (dashed). There are dielectrics below $y=0$ and above $y=0.0125$ cm. The used parameters are $d=125$ μm and 4% of Xe mole fraction.

Downloaded 12 Jun 2002 to 141.223.180.14. Redistribution subject to AIP license or copyright, see http://ojps.aip.org/pop/popcr.jsp

$$g(\mathbf{r})=\left(\int_S \frac{T(\mathbf{r},\mathbf{r}')}{4\pi|\mathbf{r}-\mathbf{r}'|^3}(\mathbf{r}-\mathbf{r}')\cdot\hat{\mathbf{n}}dA' \right)^{-1}. \quad (20)$$

In the conventional TFA, the effective decay time is approximated as $g_0\tau_v$ with the constant trapping factor of the lowest eigenmode of Holstein's solution. Molisch *et al.* calculated the value numerically and reported fitting formulas.[21] For high opacity ($k_0 d \gg 1$)

$$g_0=\frac{1}{1.146}\sqrt{\pi k_0 d}. \quad (21)$$

$g_0=132$ for the considered case.

The time evolution of the trapping factor shown in Fig. 4(b) is averaged over the Xe*($^3P_1$) density as

$$\tilde{g}(t)=\int g(\mathbf{r})n^*(\mathbf{r},t)d\mathbf{r} \Big/ \int n^*(\mathbf{r},t)d\mathbf{r}. \quad (22)$$

As shown in Fig. 4(b), $\tilde{g}(t)$ has larger value than g_0 while the discharge is sustained. It means that the density profile of the Xe*($^3P_1$) state is very different from the lowest eigenmode of the one-dimensional Holstein's solution at this time.

As mentioned above, the discharges after the second pulse, and thus in the steady state, are coplanar discharges between (X) and (Y) electrodes. Therefore, we have much interest in the coplanar discharges rather than the matrix discharge. The time evolutions of the spatially averaged density of the Xe*($^3P_1$) state and the integrated photon fluxes on the phosphor are compared in Figs. 5 and 6 for the RT calculation and the TFA method. The marked percentage is the discrepancy between the two methods obtained by the integration over one pulse period, from 5 to 10 μs.

In Fig. 5, we investigate the effect of the gap distance (d) with a fixed Xe fraction, 4%. As we increase the gap distance from 125 to 250 μm, the discrepancy increases significantly. However, if we increase the Xe mole fraction from 1% to 10% with a fixed gap distance $d=125$ μm as shown in Fig. 6, the discrepancy does not change much. In the former case, k_0 are constant because of the constant Xe mole fraction and the constant gas pressure while d varies. In the latter case, d is constant and k_0 varies from 2.3×10^5 to 8.4×10^5 cm^{-1}. Therefore, the opacity ($k_0 d$) is varied for both the cases.

The opacity is the only governing factor in the conventional TFA as shown in Eq. (21), but the effect of gap distance is more important in the RT simulation results than that of Xe mole fraction even for the same opacity. This is caused by the property of coplanar discharges, which are generated near the front plate and thus have very different profiles from the sinusoidal lowest eigenmode of Holstein's solution. The difference between the density profile and the eigenmode increases as the gap distance increases, but is independent of the Xe mole fraction. For this reason, the conventional TFA is not appropriate for a PDP cell especially when the gap distance becomes longer. However, if we use a small gap distance, e.g., 125 μm, the discrepancy is less than 3% between the two methods in the total UV photons arriving at the phosphor surface.

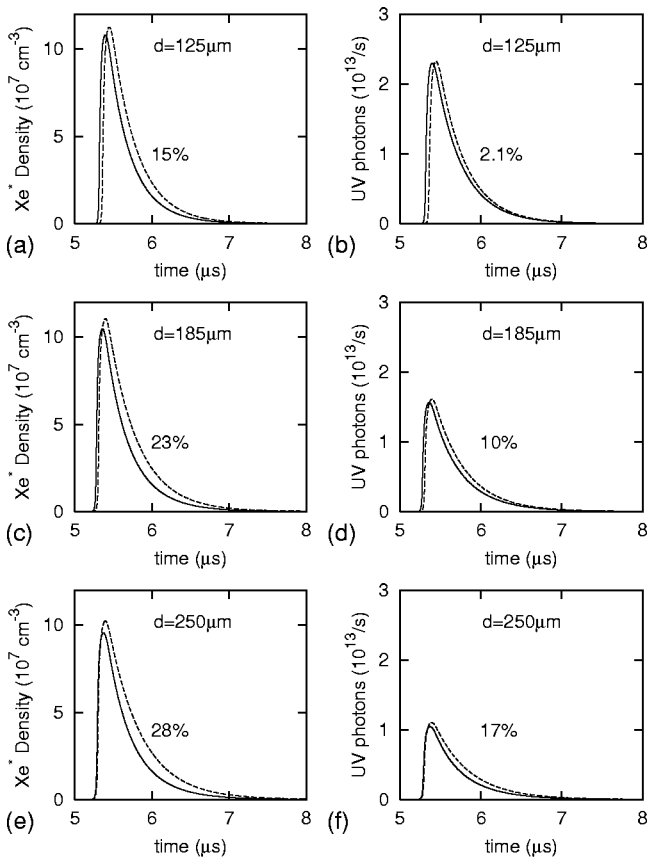

FIG. 5. Time evolutions of the average Xe*($^3P_1$) density [(a), (c), and (e)] and total UV photons arriving at the phosphor surface [(b), (d), and (f)] with the full RT calculation (solid) and the trapping factor approach (dashed) for $d=125$, 185, and 250 μm. 4% of Xe gas fraction and the applied voltage shown in Fig. 1(b) are used. The marked percentage means the difference of the quantities obtained by the two methods which are integrated over one pulse period.

In Fig. 5, the average Xe*($^3P_1$) densities are similar for the three gap distances, but the total UV photons reaching the phosphor surface decrease as d increases because the main discharge region becomes farther from the phosphor surface as d increases. As shown in Fig. 6, however, the total amount of the UV photons reaching the phosphor surface increases only slightly when we increase the Xe mole fraction from 1% to 10% while the average Xe*($^3P_1$) density increases more than twice. This is due to the increasing absorption coefficient and larger radiation trapping.

Figure 7 shows Xe*($^3P_1$) density profiles at different time for the case shown in Fig. 5(a). Before the average density is at the peak value, around $t=5.4$ μs, the production rate due to the electron impact excitation is more dominant than the radiative decay rate in right-hand side of Eq. (1), and thus two cases with the RT calculation and with the TFA show similar density profiles as shown in Figs. 7(a) and 7(b). However, after the production rate decreases because of the weakened electric field due to the accumulated wall charge on the dielectrics, the radiative decay rate is more dominant, and thus the density profiles changes a lot for the case of full RT calculation [Figs. 7(c) and 7(e)] compared with those with the TFA method [Figs. 7(d) and 7(f)]. In the considered parameter regime, the radiation transport of the Xe*($^3P_1$)

Downloaded 12 Jun 2002 to 141.223.180.14. Redistribution subject to AIP license or copyright, see http://ojps.aip.org/pop/popcr.jsp

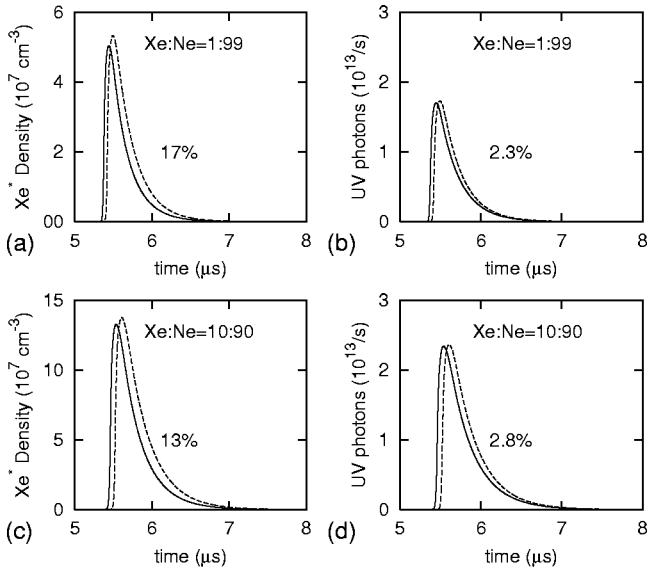

FIG. 6. Time evolutions of the average Xe*($^3P_1$) density [(a) and (c)] and total UV photons arriving at the phosphor surface [(b) and (d)] with the full RT calculation (solid) and the trapping factor approach (dashed) for 1% and 10% Xe gas fraction. The gap distance $d=125$ μm and the applied voltage shown in Fig. 1(b) are used. The marked percentage means the difference of the quantities obtained by the two methods which are integrated over one pulse period.

state is more dominant than that by diffusion, and thus it is important to include radiation transport of the resonant state in order to calculate the luminous efficiency correctly.

The spectral radiation fluxes of the UV lights on the phosphor surface are shown in Fig. 8 for different gap distances and for different Xe mole fractions. As the gap distance increases, the photon flux decreases as shown in Fig. 8(a) because the distance between the discharge region and the phosphor increases. For this case, the linewidths of the spectra are same due to the same Xe mole fraction (4%). If we change the Xe fraction, from Eq. (7), the linewidth changes. As shown in Fig. 8(b), the maximum of the spectrum is larger but the linewidth is narrower when Xe fraction is 1% compared with the case with 10%. Therefore, the total spectrum integrated over frequency is slightly larger for the

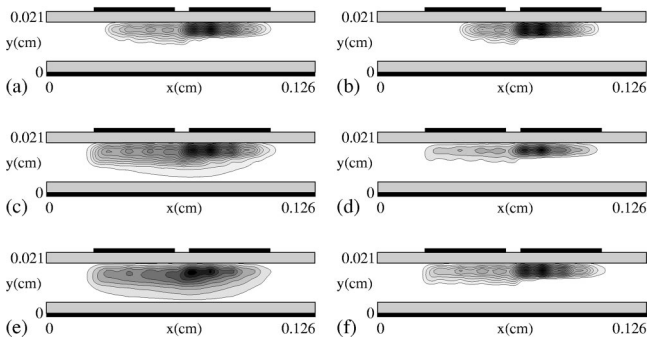

FIG. 7. Comparison of the Xe*($^3P_1$) density profiles calculated with the full RT calculation [(a), (c), and (e)] and with the TFA [(b), (d), and (f)] at 5.4 μs [(a) and (b)], 5.7 μs [(c) and (d)], and 6.0 μs [(e) and (f)]. The maximum value of each contour plot are (a) 1.2×10^{14}, (b) 1.8×10^{14}, (c) 2.2×10^{13}, (d) 6.8×10^{13}, (e) 5.5×10^{12}, and (f) 2.5×10^{13} cm^{-3}, respectively.

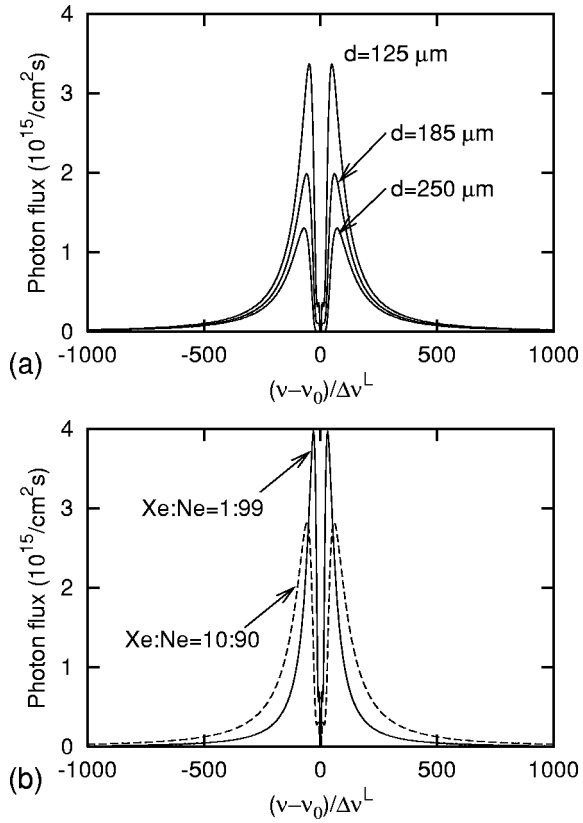

FIG. 8. Spectral radiation flux at the density peak (around $t=5.4$ μs) (a) for different gap distances with a fixed ratio, Xe:Ne=4:96, and (b) for different Xe fractions with a fixed gap distance $d=125$ μm.

10% case. The simulation results of Fig. 8 show the same tendency as the Monte Carlo simulation results and the experimental results shown in Figs. 6 and 7 of Ref. 6.

IV. SUMMARY AND DISCUSSIONS

We have presented a two-dimensional radiation transport model coupled with a fluid model to simulate a PDP cell. Holstein's equation is self-consistently solved with a propagator function method[9] for pressure broadening in the high opacity regime.

Compared with the conventional trapping factor approach, the time evolution of the average resonant state density and total radiation flux on the phosphor changes greatly as the gap distance increases, while they are not affected significantly by the change of Xe mole fraction. The spatial profile of the density also changes significantly because the density redistribution due to the radiation transport is more dominant than that due to particle diffusion. Therefore, the UV radiation flux on the phosphor differs up to 17% between the full calculation and the trapping factor approach when the gap distance is 250 μm. The discrepancy increases with an increasing gap distance. When the gap distance is short (e.g., 125 μm), however, the difference of the UV radiation flux between the two methods is less than 3%. The dependency on the gap distance is mainly due to the discrepancy between the resonant state density profile and the lowest eigenmode of the solution of Holstein's equation.

Downloaded 12 Jun 2002 to 141.223.180.14. Redistribution subject to AIP license or copyright, see http://ojps.aip.org/pop/popcr.jsp

The calculation of the spectral radiation flux is also provided in this model, and the results agree well with those of the previously reported Monte Carlo simulation and experiment.[6]

As for the simulation speed, the radiation transport calculation does not affect the simulation speed much because the radiation transport matrix [Eq. (10)] is calculated only once at the beginning of the simulation when there is no change in ground state density profile. During the evolution of the radiation transport with Eqs. (8) and (9), the transport for long distance where $A_{jk;lm}$ is less than 10^{-6} is neglected. Therefore, the number of calculations for the N×M matrix is much smaller than $(\mathrm{N}\times\mathrm{M})^2$, and the calculation time used in the RT equation is shorter than that used in Poisson's equation with a successive over-relaxation (SOR) method and continuity equations for three gas species including many excited states with a number of collisions.

In order to extend the model to a three-dimensional radiation transport model, we need to change the radiation transport matrix from $A_{jk;lm}$ to $A_{ijk;lmn}$, where (i,j,k) is the three-dimensional grid position of the absorbed photon and (l,m,n) is the emission position of the photon. For this case, Eq. (10) comes to have six surface integral segments, and the interval of the z directional integral, like the one in Eq. (A7), should be changed from $(-\infty,\infty)$ to $(0,L_z)$, where L_z is the length in z direction. The three-dimensional radiation transport model is to be our future work.

ACKNOWLEDGMENTS

This work was supported by LG Electronics and the Korea Ministry of Education through its Brain Korea 21 program.

APPENDIX A: DERIVATION OF RADIATION TRANSPORT MATRIX

The probability of a photon emitted at $\mathbf{r}'$ within the (l,m)th cell to be reabsorbed at the center of the (j,k)th cell, $\mathbf{r}_{jk}$, is defined as

$$A_{jk;lm}\equiv\int_{lm}G(\mathbf{r}_{jk},\mathbf{r}')d\mathbf{r}', \tag{A1}$$

where $\int_{lm}d\mathbf{r}'$ is a volume integral over the (l,m)th cell, and the kernel function $G(\mathbf{r},\mathbf{r}')$ is calculated from the transmission factor as

$$\begin{aligned}G(\mathbf{r},\mathbf{r}')&=-\frac{\mathbf{R}}{4\pi R^3}\cdot\nabla_{\mathbf{r}}T(\mathbf{r},\mathbf{r}')\\&=-\nabla_{\mathbf{r}}\cdot\left[\frac{\mathbf{R}}{4\pi R^3}T(\mathbf{r},\mathbf{r}')\right]+\delta^3(\mathbf{r},\mathbf{r}').\end{aligned} \tag{A2}$$

With uniform ground-state density profile, the line shape, $g(\nu,\mathbf{r})$, and the absorption coefficient, $k(\nu,\mathbf{r})$, depend only on frequency of the photons, ν, and thus the transmission factor is

$$T(R)=\int_0^\infty g(\nu)e^{-k(\nu)R}d\nu, \tag{A3}$$

where $R=|\mathbf{r}-\mathbf{r}'|$. Pressure broadening which has the Lorentz line shape is the dominant broadening mechanism in a PDP cell, and for this case, Eq. (A3) becomes[9]

$$\begin{aligned}T(R)&=\frac{\Delta\nu}{2\pi}\int_0^\infty\frac{1}{(\nu-\nu_0)^2+(\Delta\nu/2)^2}\\&\quad\times\exp\left(-\frac{k_0R}{4(\nu-\nu_0)^2/\Delta\nu^2+1}\right)d\nu\\&=\exp\left(-\frac{k_0R}{2}\right)I_0\left(\frac{k_0R}{2}\right),\end{aligned} \tag{A4}$$

where $I_0(x)$ is the zeroth-order modified Bessel function. The equation can be approximated at high opacity ($k_0R\gg1$) as

$$T(R)\simeq\frac{1}{\sqrt{\pi k_0R}}. \tag{A5}$$

From Eq. (A2) with divergence theorem

$$A_{jk;lm}=\delta_{jl}\delta_{km}+\int_{lm}\frac{T(\mathbf{r}_{jk},\mathbf{r}')}{4\pi R^3}\mathbf{R}\cdot\hat{\mathbf{n}}dS. \tag{A6}$$

The surface integral in Eq. (A6) has four segments in Cartesian coordinates as shown in Fig. 2, and each of them is defined as $A^{(a)}_{jk;lm}$, $A^{(b)}_{jk;lm}$, $A^{(c)}_{jk;lm}$, and $A^{(d)}_{jk;lm}$.

With the property of shift invariance and isotropy, it has been verified that $A_{jk;lm}$ is only a function of the distance between the positions of photon emission and reabsorption, and thus $A_{jk;lm}=A_{|j-l|,|k-m|}$. For the top boundary in Fig. 2

$$A^{(a)}_{jk;lm}=\left(y_k-y_m-\frac{\Delta y}{2}\right)\int_{x_l-\Delta x/2}^{x_l+\Delta x/2}\int_{-\infty}^{\infty}\frac{T(R)}{4\pi R^3}dx'dz' \tag{A7}$$

$$\begin{aligned}&=-\frac{\Delta y}{2\pi}\left(|k-m|+\frac{1}{2}\right)\int_{x_l-\Delta x/2}^{x_l+\Delta x/2}dx'\\&\quad\times\int_0^{\pi/2}\cos\,\theta d\theta\frac{T(R_\perp\,\sec\,\theta)}{R_\perp^2},\end{aligned} \tag{A8}$$

where $R_\perp=R\cos\,\theta=[(x_j-x')^2+(y_k-y_m-\Delta y/2)^2]^{1/2}$ and $z'=R_\perp\tan\,\theta$. With the high opacity approximation, Eq. (A5)

$$\begin{aligned}&A^{(a)}_{|j-l|,|k-m|}\\&=-\frac{\Delta y}{2\pi}\left(|k-m|+\frac{1}{2}\right)\frac{1}{\sqrt{\pi k_0}}\\&\quad\times\int_{x_l-\Delta x/2}^{x_l+\Delta x/2}\frac{1}{R_\perp^{5/2}}dx'\int_0^{\pi/2}\cos^{3/2}\,\theta d\theta\\&=-\frac{\Delta y(|k-m|+\frac{1}{2})}{12\pi^2\sqrt{2k_0}}\Gamma^2\left(\frac{1}{4}\right)\\&\quad\times\int_{(|j-l|-1/2)\Delta x}^{(|j-l|+1/2)\Delta x}\left[x^2+\Delta y^2\left(|k-m|+\frac{1}{2}\right)^2\right]^{-5/4}dx,\end{aligned} \tag{A9}$$

Downloaded 12 Jun 2002 to 141.223.180.14. Redistribution subject to AIP license or copyright, see http://ojps.aip.org/pop/popcr.jsp

which is just a single integral over position x. Here, $\Gamma(1/4)=3.6256\cdots$ is a specific value of the gamma function and comes from the relation

$$\int_0^{\pi/2}\cos^{3/2}\theta d\theta=\frac{1}{6\sqrt{2\pi}}\Gamma^2\left(\frac{1}{4}\right). \tag{A10}$$

For the bottom boundary

$$A^{(c)}_{jk;lm}=\frac{\Delta y(|k-m|-1/2)}{12\pi^2\sqrt{2k_0}}\Gamma^2\left(\frac{1}{4}\right)\times\int_{(|j-l|-1/2)\Delta x}^{(|j-l|+1/2)\Delta x}\left[x^2+\Delta y^2\left(|k-m|-\frac{1}{2}\right)^2\right]^{-5/4}dx. \tag{A11}$$

In a similar way, for the right-hand side boundary

$$A^{(b)}_{jk;lm}=-\frac{\Delta x(|j-l|+1/2)}{12\pi^2\sqrt{2k_0}}\Gamma^2\left(\frac{1}{4}\right)\times\int_{(|k-m|-1/2)\Delta y}^{(|k-m|+1/2)\Delta y}\left[y^2+\Delta x^2\left(|j-l|+\frac{1}{2}\right)^2\right]^{-5/4}dy, \tag{A12}$$

and for the left-hand side boundary

$$A^{(d)}_{jk;lm}=\frac{\Delta x(|j-l|-1/2)}{12\pi^2\sqrt{2k_0}}\Gamma^2\left(\frac{1}{4}\right)\times\int_{(|k-m|-1/2)\Delta y}^{(|k-m|+1/2)\Delta y}\left[y^2+\Delta x^2\left(|j-l|+\frac{1}{2}\right)^2\right]^{-5/4}dy. \tag{A13}$$

Finally,

$$A_{jk;lm}=\delta_{jl}\delta_{km}+A^{(a)}_{|j-l|,|k-m|}+A^{(b)}_{|j-l|,|k-m|}+A^{(c)}_{|j-l|,|k-m|}+A^{(d)}_{|j-l|,|k-m|}. \tag{A14}$$

APPENDIX B: DERIVATION OF SPECTRAL RADIATION FLUX

At the back plate, spectral photon flux is calculated as

$$F(\mathbf{r},\nu)=\frac{1}{4\pi}\int_{V'}\frac{S_r(\mathbf{r}')g(\nu)\exp[-k(\nu)|\mathbf{r}-\mathbf{r}'|]}{|\mathbf{r}-\mathbf{r}'|^2}\hat{\mathbf{R}}\cdot\hat{\mathbf{n}}dV', \tag{B1}$$

where $\mathbf{r}=(x_i,y_0,0)$ is a location on the phosphor surface, V' is the volume of the plasma region, and $S_r(\mathbf{r}')$ is the photon emission rate defined as

$$S_r(\mathbf{r}')=n^*(\mathbf{r}')/\tau_v. \tag{B2}$$

With the piecewise constant approximation

$$F(x_i,\nu)=\frac{g(\nu)}{4\pi}\sum_{j=1}^{N_x}\sum_{k=1}^{N_y}S_r(x_j,y_k)\int_{x_j-\Delta x/2}^{x_j+\Delta x/2}dx'\times\int_{y_k-\Delta y/2-y_0}^{y_k+\Delta y/2-y_0}dy'\int_{-\infty}^{\infty}dz'y'\times\frac{\exp[-k(\nu)\sqrt{(x_i-x')^2+y'^2+z'^2}]}{[(x_i-x')^2+y'^2+z'^2]^{3/2}}. \tag{B3}$$

If we consider three-dimensional distribution of the excited state, the infinite range of z directional integral should be changed to a finite range. However, we assume infinitely long z length with only two-dimensional distribution.

With $R_\perp=\sqrt{(x_i-x')^2+y'^2}$, $R=R_\perp\sec\theta$, and $z'=R_\perp\tan\theta$,

$$F(x_i,\nu)=\frac{g(\nu)}{4\pi}\sum_{j=1}^{N_x}\sum_{k=1}^{N_y}S_r(x_j,y_k)\times\int_{x_j-\Delta x/2}^{x_j+\Delta x/2}\int_{y_k-\Delta y/2-y_0}^{y_k+\Delta y/2-y_0}y'\frac{1}{R_\perp^2}\times\int_0^{\pi/2}\exp[-k(\nu)R_\perp\sec\theta]\cos\theta d\theta dy'dx'. \tag{B4}$$

With the relation that

$$\int_0^{\pi/2}\cos\theta\exp(-\alpha\sec\theta)d\theta=\int_0^{\infty}\frac{\exp(-\alpha\cosh z)}{\cosh^2 z}dz=Ki_2(\alpha), \tag{B5}$$

$$F(x_i,\nu)=\frac{g(\nu)}{4\pi}\sum_{j=1}^{N_x}\sum_{k=1}^{N_y}S_r(x_j,y_k)\times\int_{x_j-\Delta x/2}^{x_j+\Delta x/2}\int_{y_k-\Delta y/2-y_0}^{y_k+\Delta y/2-y_0}y'\times\frac{Ki_2[k(\nu)\sqrt{(x_i-x')^2+y'^2}]}{(x_i-x')^2+y'^2}dy'dx', \tag{B6}$$

where $Ki_2(x)$ is the second repeated integral of the zeroth-order modified Bessel function, $K_0(x)$.[20] However, Eq. (B6) needs huge computations, and thus we calculate it using average distance between the phosphor surface and the center of the cell where a photon is emitted, which is defined as R_0. If R_0 is enough larger than Δx and Δy, we can pull $\mathbf{R}\cdot\hat{\mathbf{n}}$ out of the volume integral in Eq. (B1), and thus

$$F(\mathbf{r},\nu)=\frac{1}{4\pi}\mathbf{R}_0\cdot\hat{\mathbf{n}}\int_{V'}\frac{S_r(\mathbf{r}')g(\nu)\exp[-k(\nu)|\mathbf{r}-\mathbf{r}'|]}{|\mathbf{r}-\mathbf{r}'|^3}dV'=\frac{g(\nu)}{4\pi}\sum_j\sum_k S_r(x_j,x_k)\mathbf{R}_0\cdot\hat{\mathbf{n}}\frac{1}{R_{\perp 0}^2}\times Ki_2[k(\nu)R_{\perp 0}]\Delta x\Delta y. \tag{B7}$$

Finally

Downloaded 12 Jun 2002 to 141.223.180.14. Redistribution subject to AIP license or copyright, see http://ojps.aip.org/pop/popcr.jsp

$$F(x_i,\nu)=\frac{g(\nu)}{4\pi}\sum_{j=1}^{N_x}\sum_{k=1}^{N_y}S_r(x_j,y_k)(y_k-y_0)\times\frac{Ki_2[k(\nu)\sqrt{(x_j-x_i)^2+(y_k-y_0)^2}]}{(x_j-x_i)^2+(y_k-y_0)^2}\Delta x\Delta y \tag{B8}$$

$$=\sum_{j=1}^{N_x}\sum_{k=1}^{N_y}n_{jk}^{*}\tilde{F}^{\nu}{}_{|i-j|,k}, \tag{B9}$$

where

$$\tilde{F}^{\nu}{}_{|i-j|,k}=\frac{g(\nu)}{4\pi\tau_v}\Delta x\Delta y(y_k-y_0)\times\frac{Ki_2[k(\nu)\sqrt{(x_j-x_i)^2+(y_k-y_0)^2}]}{(x_j-x_i)^2+(y_k-y_0)^2}. \tag{B10}$$

APPENDIX C: DERIVATION OF TOTAL RADIATION FLUX

The total photon flux is

$$F(\mathbf{r})=\int_0^{\infty}F(\mathbf{r},\nu)d\nu. \tag{C1}$$

From the integral of Eq. (A3) over frequency ν

$$F(\mathbf{r})=\frac{1}{4\pi}\int_{V'}\frac{S_r(\mathbf{r}')T(|\mathbf{r}-\mathbf{r}'|)}{|\mathbf{r}-\mathbf{r}'|^2}\hat{\mathbf{R}}\cdot\hat{\mathbf{n}}dV'. \tag{C2}$$

With a high opacity approximation, $T(R)=(\pi k_0R)^{-1/2}$

$$F(x_i)=\frac{1}{4\pi\sqrt{\pi k_0}}\int_{V'}\frac{S_r(\mathbf{r}')}{R^{7/2}}\mathbf{R}\cdot\hat{\mathbf{n}}dV'$$
$$=\frac{1}{4\pi\sqrt{\pi k_0}}\sum_{j=1}^{N_x}\sum_{k=1}^{N_y}S_r(x_j,y_k)\int_{x_j-\Delta x/2}^{x_j+\Delta x/2}dx'\times\int_{y_k-\Delta y/2-y_0}^{y_k+\Delta y/2-y_0}dy'\int_{-\infty}^{\infty}dz'y'\times[(x_i-x')^2+y'^2+z'^2]^{-7/4}. \tag{C3}$$

With substitution of $z'=R_{\perp}\tan\theta$ and $t=y'^2$, and utilizing $\int_0^{\pi/2}\cos^{3/2}\theta d\theta=\Gamma^2(1/4)/6\sqrt{2\pi}$

$$F(x_i)=\frac{\Gamma^2(1/4)}{6\pi^2\sqrt{2k_0}}\sum_{j=1}^{N_x}\sum_{k=1}^{N_y}S_r(x_j,y_k)\times\int_{x_j-\Delta x/2}^{x_j+\Delta x/2}\{[(x_i-x')^2+(y_k-\Delta y/2-y_0)^2]^{-1/4}-[(x_i-x')^2+(y_k+\Delta y/2-y_0)^2]^{-1/4}\}dx' \tag{C4}$$

$$=\sum_{j=1}^{N_x}\sum_{k=1}^{N_y}n_{jk}^{*}F_{|i-j|,k}, \tag{C5}$$

where

$$F_{|i-j|,k}=\frac{\Gamma^2(1/4)}{6\pi^2\tau_v\sqrt{2k_0}}\times\int_0^{\Delta x/2}\{[(|x_i-x_j|+x')^2+(y_k-y_0)^2]^{-1/4}+[(|x_i-x_j|-x')^2+(y_k-y_0)^2]^{-1/4}-[(|x_i-x_j|+x')^2+(y_k-y_0+\Delta y)^2]^{-1/4}-[(|x_i-x_j|-x')^2+(y_k-y_0+\Delta y)^2]^{-1/4}\}dx'. \tag{C6}$$

[1] J. K. Lee and J. P. Verboncoeur, *Lectures in Plasma Science and Plasma Technology* (Wiley-VCH, Berlin, 2001), pp. 6–24.
[2] A. Sobel, IEEE Trans. Plasma Sci. **19**, 1032 (1991).
[3] *Electronic Display Devices*, edited by S. Matsumoto (Wiley, New York, 1990), p. 131.
[4] J. A. Castelano, *Handbook of Display Technology* (Academic, New York, 1992), p. 111.
[5] T. Holstein, Phys. Rev. **72**, 1213 (1947); **83**, 1159 (1951).
[6] G. J. M. Hagelaar, M. H. Klein, R. J. M. M. Snijkers, and G. M. W. Kroesen, J. Appl. Phys. **88**, 5538 (2000).
[7] T. Straaten and M. J. Kushner, J. Appl. Phys. **87**, 2700 (2000).
[8] A. F. Molisch, B. P. Oehry, W. Schupita, and G. Magerl, Comput. Phys. Commun. **93**, 127 (1993).
[9] J. E. Lawler, G. J. Parker, and W. N. G. Hitchon, J. Quant. Spectrosc. Radiat. Transf. **49**, 627 (1993).
[10] O. Sahni, C. Lanza, and W. E. Howard, J. Appl. Phys. **49**, 2365 (1978).
[11] H. J. Lee and J. P. Verboncoeur, Phys. Plasmas **8**, 3077 (2001).
[12] H. J. Lee and J. P. Verboncoeur, Phys. Plasmas **8**, 3089 (2001).
[13] H. J. Lee and J. P. Verboncoeur, J. Appl. Phys. **90**, 4957 (2001).
[14] C. K. Birdsall and A. B. Langdon, *Plasma Physics via Computer Simulation* (Adam Hilger, Bristol, 1991).
[15] Y. K. Shin, C. H. Shon, W. Kim, and J. K. Lee, IEEE Trans. Plasma Sci. **27**, 1366 (1999).
[16] J. Meunier, P. Belenguer, and J. P. Boeuf, J. Appl. Phys. **78**, 731 (1995).
[17] S. Rauf and M. J. Kushner, J. Appl. Phys. **85**, 3460 (1999).
[18] H. C. Kim, M. S. Hur, S. S. Yang, S. W. Shin, and J. K. Lee, "Three-dimensional fluid simulation of a plasma display panel cell," J. Appl. Phys. (to be published).
[19] K. Igarashi, S. Mikoshiba, Y. Watanabe, M. Suzuki, and S. Murayama, J. Phys. D **28**, 1377 (1985).
[20] M. Abramowitz and I. A. Stegun, *Handbook of Mathematical Functions* (Dover, New York, 1965), p. 483.
[21] A. F. Molisch, B. P. Oehry, W. Schupita, and G. Magerl, J. Quant. Spectrosc. Radiat. Transf. **48**, 377 (1992).

Downloaded 12 Jun 2002 to 141.223.180.14. Redistribution subject to AIP license or copyright, see http://ojps.aip.org/pop/popcr.jsp